Chemical Science

ROYAL SOCIETY OF CHEMISTRY

EDGE ARTICLE

View Article Online
View Journal | View Issue

Cite this: *Chem. Sci.*, 2025, **16**, 10273

All publication charges for this article have been paid for by the Royal Society of Chemistry

Received 15th February 2025
Accepted 5th May 2025

DOI: 10.1039/d5sc01200g

rsc.li/chemical-science

Arylation of gold nanoclusters and insights into structure-related CO_2 reduction reaction performances†

Chen Zhu,‡[a] Bo Li,‡[b] Chen Li,[a] Luyao Lu,[a] Hao Li,[a] Xinhua Yuan,[a] Xi Kang,*[a] De-en Jiang*[b] and Manzhou Zhu*[a]

Research on arylgold complexes and ligand-protected gold nanoclusters has proceeded independently thus far due to the difficulty in controllably introducing aryl groups to synthesize arylgold nanoclusters. Herein we synthesized an arylgold Au_{15} nanocluster, $Au_{15}(DPPOE)_3(S\text{-}Ph^pMe)_4(Ph)_2$, thereby bridging the two independent research fields. Tetraarylborates were exploited as arylating agents to transfer aryl groups onto the nanocluster kernel, triggering the arylation of the Au_{15} cluster while maintaining the molecular framework. Furthermore, two other arylgold Au_{15} nanoclusters with halogenated surfaces were controllably synthesized by substituting the arylating agent $NaBPh_4$ with its benzene ring-halide derivatives. In addition, the change in the electronic structure from Au-SR to Au-aryl and the energetics of the arylation process from Au_{15}-SR to Au_{15}-Ph were elucidated computationally. Furthermore, the catalytic capability of the two Au_{15} nanoclusters with nuanced ligand differences was investigated in the electrochemical reduction of CO_2, and the comparable reactivity of the two cluster-based nanocatalysts was theoretically rationalized. Our findings have cross-fertilized the fields of arylgold complexes and gold nanoclusters, pointing toward a new avenue of exploration for novel arylgold nanoclusters.

1 Introduction

Gold nanoclusters have received extensive attention due to their consistently monodisperse sizes and accurately characterized structures.[1–6] These ultrasmall gold nanoparticles exhibit strong quantum-confinement effects and discrete electronic energy levels, which are manifested in their structure-dependent physicochemical properties.[7–16] Structurally, gold nanoclusters consist of metallic kernels containing "free electrons" that are protected by motif surfaces that include "peripheral ligands".[17–20] Among them, the peripheral ligands play a significant role in directing the surface chemistry of metal nanoclusters, which further determines their intracluster structures, intercluster interactions, and physicochemical properties.[21–25] To date, several types of peripheral ligands have been employed to stabilize gold nanoclusters, including thiolate,[26–28] phosphine,[29–31] halogens,[32–34] alkynyl,[35–37] carbene,[38–40] and pyridine.[41,42] Due to the diverse binding capacities and coordination modes between different peripheral ligands and gold atoms, ligand engineering, as well as ligand exchange, has served as a versatile approach for regulating the electronic/geometric structures of gold nanoclusters.[43,44]

The construction of gold nanoclusters is always associated with the reduction of their Au^I complexes; for example, the relationships between Au^I-PPh_3 complexes and phosphine-stabilized clusters,[45,46] $Au_x^I(SR)_y$ complexes and thiolate-stabilized clusters,[47,48] $Au_x^I(C{\equiv}R)_y$ complexes and alkynyl-stabilized clusters,[49] *etc.* The chemistry of arylgold has been developed for more than half a century to anchor arene groups onto gold atoms, giving rise to arylgold complexes with widespread applications in catalysis and emitting devices.[50–54] However, little has been achieved in constructing arylgold complex-related arylgold nanoclusters that contain Au^0 kernels and free electrons. To our knowledge, there is only one case of arylgold nanoclusters being achieved through ligand exchange with a maintained template—the neutral $Au_{10}(C_6F_5)_4(PPh_3)_5$, prepared by reacting $Au_9(PPh_3)_8$ with arylgold $Au(C_6F_5)_2$ complexes, and the phenyl-stabilized Au_{44} was synthesized directly *via* a one-pot reducing procedure.[55,56] The attainment of arylated gold nanoclusters with atomic precision is highly desirable to expand their research scope and allow the fabrication of new cluster members with novel structures, compositions and performances. One idea is to leverage the knowledge

[a]*Department of Chemistry and Centre for Atomic Engineering of Advanced Materials, Key Laboratory of Structure and Functional Regulation of Hybrid Materials of Ministry of Education, Anhui Province Key Laboratory of Chemistry for Inorganic/Organic Hybrid Functionalized Materials, Anhui University, Hefei, Anhui 230601, P. R. China. E-mail: kangxi_chem@ahu.edu.cn; zmz@ahu.edu.cn*

[b]*Department of Chemical and Biomolecular Engineering, Vanderbilt University, 2301 Vanderbilt Place, Nashville, Tennessee, USA. E-mail: de-en.jiang@vanderbilt.edu*

† Electronic supplementary information (ESI) available: Fig. S1–S33 and Tables S1–S5. CCDC 2307548–2307550. For ESI and crystallographic data in CIF or other electronic format see DOI: https://doi.org/10.1039/d5sc01200g

‡ C. Z. and B. L. contributed equally to this work.

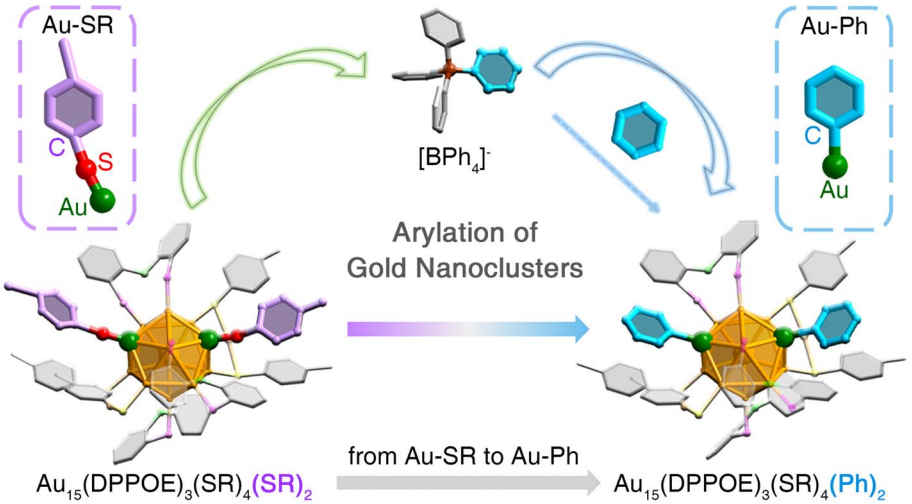

Scheme 1 Illustration of the arylation of gold nanoclusters. The $Au_{15}(DPPOE)_3(SR)_6$ cluster precursor undergoes arylation to produce the arylgold $Au_{15}(DPPOE)_3(SR)_4(Ph)_2$ nanocluster in the presence of $[BPh_4]^-$.

and chemistry of arylgold complexes. Indeed, tetraarylborates or their derivatives have been extensively exploited for the construction of arylgold complexes (or other arylmetal complexes) *via* C–B bond cleavage followed by aryl-gold bond formation;[57–59] however, whether such an arylation strategy works for arylgold nanoclusters remains unexplored.

In this work, we report the arylation of gold nanoclusters (Scheme 1). The starting $[Au_{15}(DPPOE)_3(S\text{-}Ph^pMe)_6]^+$ nanocluster (Au_{15}-SR for short; DPPOE = bis(2-diphenylphosphinophenyl)ether] has two weak surface Au-SPh^pMe bonds. The introduction of $NaBPh_4$ into the solution of Au_{15}-SR results in the cleavage of C–B bonds of $[BPh_4]^-$, triggered by cluster catalysis. The dissociated phenyl groups attack the two weak Au–S bonds on Au_{15}-SR and displace the corresponding two S-Ph^pMe groups from the cluster surface, leading to the generation of an arylgold $[Au_{15}(DPPOE)_3(S\text{-}Ph^pMe)_4(Ph)_2]^+$ nanocluster (Au_{15}-Ph for short). We further show that this approach can also be used to synthesize arylgold cluster derivatives, $[Au_{15}(DPPOE)_3(S\text{-}Ph^pMe)_4(Ph\text{-}F)_2]^+$ and $[Au_{15}(DPPOE)_3(S\text{-}Ph^pMe)_4(Ph\text{-}Cl)_2]^+$ (Au_{15}-Ph-F and Au_{15}-Ph-Cl for shorts, respectively). In addition, we employ computational chemistry to understand the driving force behind the ligand displacement reaction on the cluster surface from Au-SR to Au-aryl. Besides, the catalytic performances of the two Au_{15} cluster-based nanocatalysts in the CO_2 reduction reaction were investigated experimentally and theoretically. Overall, the findings of this work provide impetus for future experimental and theoretical developments in arylgold nanoclusters.

2 Results and discussion

The Au_{15}-SR nanocluster was prepared by a one-pot synthetic procedure *via* reducing the Au-SR-DPPOE complexes with $NaBH_4$ (see the ESI for more details; Fig. S1†). Despite several attempts, the crystallization and structural determination of the Au_{15}-SR nanocluster were unsuccessful due to its instability, which was evaluated by monitoring its optical absorption as a function of time at room temperature. As shown in Fig. S2,† the characteristic UV-vis absorptions of Au_{15}-SR gradually decreased in intensity after three hours and completely disappeared within 24 hours, indicating degradation. With the help of electrospray ionization-mass spectrometry (ESI-MS) and thermogravimetric analysis (TGA), we determined the chemical formula of the nanocluster to be $[Au_{15}(DPPOE)_3(S\text{-}Ph^pMe)_6]^+$ (Fig. S3 and S4†). To further confirm the valence state of Au_{15}-SR, we performed ESI-MS with the addition of Cs^+ cations. The mass results were consistent with those obtained without Cs^+, further confirming the chemical formula of the Au_{15}-SR nanocluster as $[Au_{15}(DPPOE)_3(S\text{-}Ph^pMe)_6]^+$ (Fig. S5†).

Inspired by the arylation of tetraarylborates in constructing arylgold complexes, we attempted to anchor the aryl groups onto the Au_{15}-SR surface to substitute them for the two detachable thiolate ligands. As shown in Fig. 1A, $NaBPh_4$ was used as the arylating agent to stabilize the Au_{15} cluster framework (see more synthetic details in the ESI†). The ESI-MS results suggested the transformation of the nanocluster from Au_{15}-SR to Au_{15}-Ph as well as the substitution of the two detachable thiolate ligands with phenyl groups on the nanocluster surface (Fig. 1B and S6†), demonstrating the successful arylation of the Au_{15} nanocluster. Of note, in the only one reported case of the arylgold nanocluster, $Au_{10}(C_6F_5)_4(PPh_3)_5$, the arylation was achieved by introducing arylgold complexes into the nanocluster precursor, which altered the cluster framework. By comparison, we herein accomplished the template-maintained arylation of gold nanoclusters through a simple ligand-exchange-triggered arylation approach.

The optical absorptions of the Au_{15}-SR and Au_{15}-Ph nanoclusters were compared. An intense optical absorption peak for Au_{15}-SR was detected at 355 nm (Fig. 1C). Following the cluster arylation, the 355 nm signal remained unchanged, and a characteristic band appeared at 410 nm. Optical absorption was also observed for the crystal of Au_{15}-Ph with a similar peak intensity, demonstrating the high conversion efficiency of the cluster

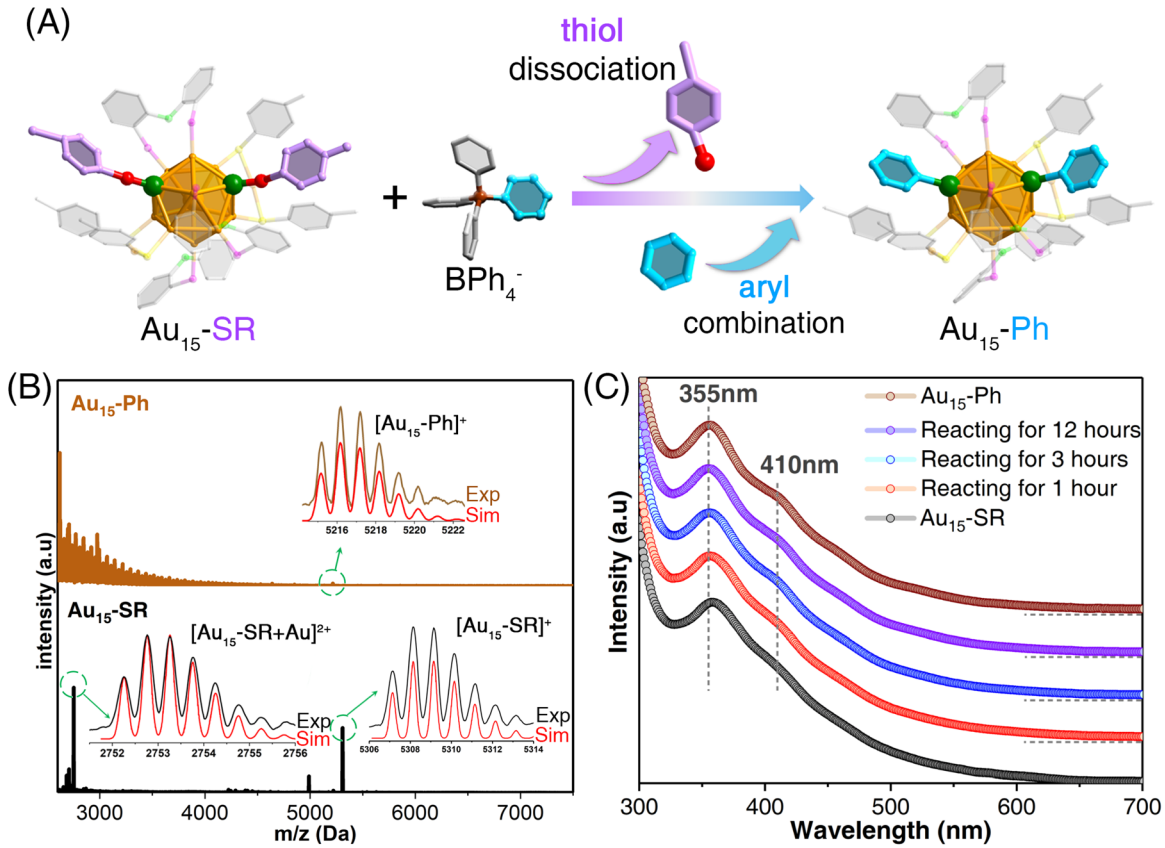

Fig. 1 Arylation of the gold nanocluster. (A) Scheme illustrating the arylation of the Au_{15}-SR precursor to produce the arylgold Au_{15}-Ph nanocluster in the presence of $[BPh_4]^-$. Accompanying the cluster arylation, two thiolate ligands of Au_{15}-SR were detached, and two aryl ligands were anchored onto the cluster surface. Color labels: orange/green = Au; yellow/red = S; magenta = P; green = O; grey = C; pink = C of the detachable thiolate ligands; cerulean = C of the aryl ligands. Some C and H atoms are omitted for clarity. (B) ESI-MS results of the Au_{15}-SR precursor and the arylgold Au_{15}-Ph nanocluster in the presence of $NaBPh_4$. The stray mass signals at ~3000 Da stemmed from the introduction of $[BPh_4]^-$, which were absent in the mass spectrum of the Au_{15}-Ph cluster (Fig. S6†). (C) Time-dependent optical absorption spectra of the transformation from Au_{15}-SR to Au_{15}-Ph.

arylation. More importantly, the arylgold Au_{15}-Ph displayed a robust cluster template that enabled crystallization (Fig. S7†), and the atomically precise structure of this arylgold nanocluster could be determined. Additionally, the stability of Au_{15}-Ph in O_2, at various temperatures, and in different solvents was tested. The nanocluster exhibited good stability in the presence of oxygen and in different solvents. However, the nanocluster decomposed gradually when the temperature exceeded 70 °C (Fig. S8†). Besides, the cyclic voltammetry tests of Au_{15}-SR and Au_{15}-Ph nanoclusters demonstrated that the energy gap between the first oxidation peak and the first reduction peak increased upon arylation of the gold nanocluster (Fig. S9†), which was consistent with the trend observed for the calculated HOMO–LUMO gap of the two nanoclusters (discussed below).

Structurally, the Au_{15}-Ph nanocluster contained an icosahedral Au_{13} kernel (Fig. 2A), which was enwrapped by three bidentate DPPOE ligands and two dimeric $Au_1(SR)_2$ motif structures *via* Au–P and Au–S interactions, respectively, giving rise to an $Au_{15}(DPPOE)_3(SR)_4$ structure (Fig. 2B–D). In this context, of the 12 surface Au atoms on this Au_{13} kernel, six Au atoms and four Au atoms were capped by phosphine and thiol ligands, respectively, while two Au atoms remained bare on $Au_{15}(DPPOE)_3(SR)_4$ (Fig. 2D). Two aryl ligands, originating from the arylating agent $NaBPh_4$, further stabilized the remaining two bare Au atoms, completing the overall structure of the arylgold Au_{15}-Ph nanocluster (Fig. 2E–G). Considering their similar optical absorptions, we propose that the Au_{15}-SR and Au_{15}-Ph nanoclusters exhibited the same cluster framework; accordingly, the two detachable thiolate ligands of Au_{15}-SR should also anchor onto its Au_{13} kernel independently, and their dissociation would expose the cluster kernel directly to the external environment, leading to the instability of the nanocluster. In contrast, the aryl ligands adhered onto the Au_{15}-Ph cluster surface firmly with the assistance of several intracluster C–H···π interactions (Fig. 2H). Specifically, three types of C–H···π interactions were detected, including (i) the type I interaction between C–H from aryl ligands and π from phosphine ligands (Fig. 2I), (ii) the type II interaction between C–H from thiol ligands and π from aryl ligands, and (iii) the type III interaction between C–H from aryl ligands and π from thiol ligands (Fig. 2J). Collectively, each aryl ligand was locked by a combination of adjacent DPPOE and $Au_1(SR)_2$ ligands *via*

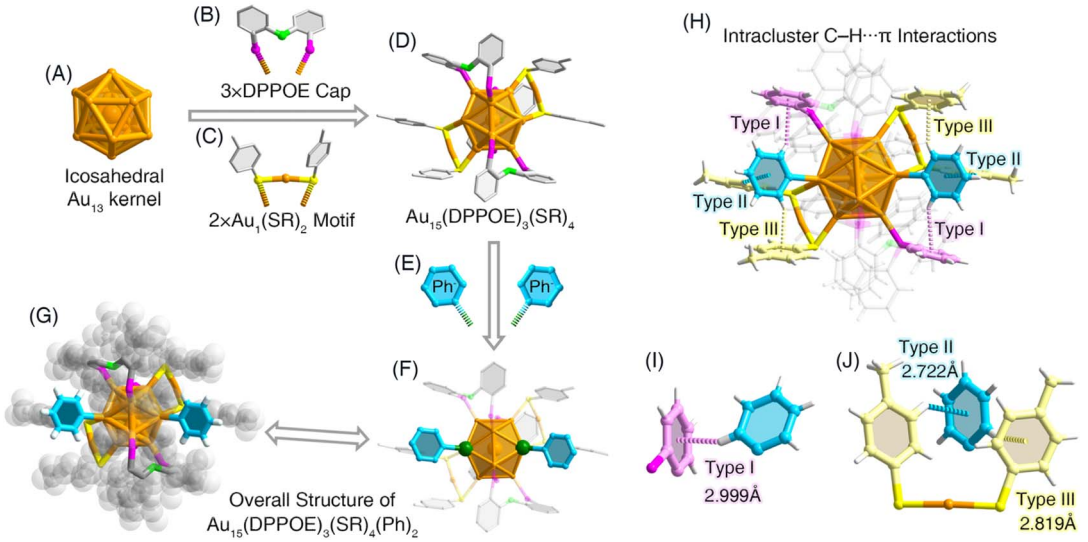

Fig. 2 Structural anatomy of the arylgold Au_{15}-Ph nanocluster. (A) The innermost icosahedral Au_{13} kernel. (B) The bidentate DPPOE cap. (C) The dimeric $Au_1(SR)_2$ motif. (D) The $Au_{15}(DPPOE)_3(SR)_4$ structure. (E) The aryl ligand. (F and G) The overall structure of the Au_{15}-Ph nanocluster. (H–J) The intracluster C–H···π interactions stabilizing the aryl ligands on the nanocluster surface. The interactions are highlighted in colors corresponding to the π-donating groups. Color labels: orange/green = Au; yellow = S; magenta = P; green = O; grey = C; cerulean = C of the aryl ligands; pale magenta = C of the phosphine ligands; pale yellow = C of the thiol ligands; white = H. Some C and H atoms are omitted for clarity.

multiple C–H···π interactions, realizing the high robustness of the Au_{15}-Ph framework. In addition, we compared the bond lengths of the standard Au_{13} nanocluster with those of Au_{15}-Ph and found that the Au_{13} kernel was more tightly arranged than that of Au_{15}-Ph (Table S4†).

We further expanded the cluster system of arylgold Au_{15} by substituting the arylating agent $[BPh_4]^-$ with its benzene ring-halide derivatives—$[B(Ph\text{-}F)_4]^-$ and $[B(Ph\text{-}Cl)_4]^-$. As shown in Fig. S10 and S11,† the ESI-MS and UV-vis results demonstrated the successful arylation of Au_{15}-SR and the generation of $[Au_{15}(DPPOE)_3(S\text{-}Ph^pMe)_4(Ph\text{-}F)_2]^+$ and $[Au_{15}(DPPOE)_3(S\text{-}Ph^pMe)_4(Ph\text{-}Cl)_2]^+$ (Au_{15}-Ph-F and Au_{15}-Ph-Cl for short, respectively). All three arylgold Au_{15} nanoclusters exhibited the same molecular composition, $[Au_{15}(DPPOE)_3(S\text{-}Ph^pMe)_4(Ph\text{-}X)_2]^+$ (X = H, F, or Cl), suggesting their closed-shell electronic structures with a nominal electron count of eight (*i.e.*, 15 (Au) − 4 (SR) − 2 (Ph-X) − 1 (charge) = 8), tallying with the icosahedral unit in the cluster framework. Besides, the X-ray photoelectron spectroscopy (XPS) results showed that the binding energies of Au_{4f} in the three arylgold nanoclusters showed remarkable blue-shifts relative to Au_{15}-SR. (Fig. S12†). The stability of these Au_{15} nanoclusters bearing different aryl groups was analyzed, and both Au_{15}-Ph-F and Au_{15}-Ph-Cl exhibited excellent stability over 24 hours (Fig. S13†). Structurally, the Au_{15}-Ph-F and Au_{15}-Ph-Cl clusters displayed analogous geometric structures and intramolecular interactions to their initial arylgold Au_{15}-Ph nanocluster (Fig. S14 and S15†); however, due to the substituent effects on the aryl ligands, the three clusters expressed slight differences in terms of their atomic packing and bond lengths. Specifically, the icosahedral Au_{13} kernels of the three nanoclusters were similar, considering their analogous average lengths of Au(icosahedral core)–Au(icosahedral core) and Au(icosahedral core)–Au(icosahedral surface) bonds (Fig. S16†). However, for the kernel–shell interactions of the cluster framework, a closer interaction was detected for both Au_{15}-Ph-F and Au_{15}-Ph-Cl relative to the Au_{15}-Ph nanocluster due to the shortened bond lengths between Au atoms on the icosahedral surface and S/P/C atoms from peripheral ligands (Fig. S17 and S18†). In this context, the substituent group (*i.e.*, F or Cl) increased the electron-withdrawing capability of the aryl ligand and strengthened the interactions between gold kernels of nanoclusters and peripheral ligands. Besides, the substituent effects also influenced the crystalline packing of these arylgold nanoclusters (Fig. S19†)—although all three cluster entities were crystallized in a triclinic crystal system with a $P\bar{1}$ space group, they exhibited different crystalline parameters, including cell lengths, cell angles, crystal densities, *etc.*

For the preparation of arylgold complexes (or other arylmetal complexes), tetraarylborates were extensively exploited as arylating agents to deliver aromatic groups *via* C–B bond cleavage. For the arylation process from Au_{15}-SR to Au_{15}-Ph, the initiation reaction should be the C–B bond cleavage of $[BPh_4]^-$ catalyzed by the nanocluster, the same as the reaction between gold complexes and borate species (Fig. S20†).[60,61] Indeed, the nuclear magnetic resonance (NMR) and gas chromatography mass spectrometry (GC-MS) results identified BPh_3 and biphenyl as by-products of the nanocluster arylation, which were considered as fragment products from the C–B bond cleavage of $[BPh_4]^-$ (Fig. S21–S24†). Besides, the GC results also identified the presence of benzene in the by-product (Fig. S25†). Interestingly, the Au_{15}-SR nanocluster could catalyze the C–B bond cleavage of tetraarylborates, which further contributed to the nanocluster arylation. However, for the reported nanoclusters with similar thiol and DPPOE ligands, no C–B bond

cleavage of the introduced $[BPh_4]^-$ was observed (Fig. S26†).[62] Indeed, the introduction of $[BPh_4]^-$ in previous cluster research aimed at substituting small-sized counterions (*e.g.*, Cl^-) in positively charged nanoclusters for facilitating their crystallization. In this work, the two detachable thiolate ligands on Au_{15}-SR led to its instability, while, the partially exposed gold kernel might endow the cluster molecule with high catalytic capacity towards the C–B bond cleavage of tetraarylborates. In addition, the dissociated aryl group from $[BPh_4]^-$ further activated the Au_{15}-SR molecule, triggering the complete dissociation of the two detachable thiolate ligands on the cluster surface by anchoring onto these two positions *via* Au–aryl interactions, giving rise to the final arylgold Au_{15}-Ph nanocluster (Fig. S20†). In this context, the arylation of this Au_{15} cluster template could be accomplished. Of note, the Au–aryl interactions in Au_{15}-Ph were much more robust than the Au–S interactions at the two ligand-exchanging sites, and the anti-arylation from Au_{15}-Ph to Au_{15}-SR was not successful (Fig. S27†).

To understand the thermodynamic driving force of the arylation process from Au_{15}-SR to Au_{15}-Ph, we employed density functional theory (DFT) calculations to calculate the reaction energy of the arylation process (see the ESI† for more details). Modelling the complete arylation process required determining the speciation of the side products involving SR, which was challenging due to the high complexity of the reaction system. To simplify the process, we used the phenyl group and the thiolate group in their radical states; in other words, the reaction was a measure of the relative binding energy of Au_{15}-Ph *versus* Au_{15}-SR. The structure of the Au_{15}-Ph was taken from its crystal structure and the Au_{15}-SR cluster was built by substituting -SR for the two -Ph groups. Geometry optimizations were performed before calculating the reaction energy. For Au_{15}-Ph, the DFT optimized structure shows a small deviation (RMSD = 0.4 Å) compared to the crystal structure. The calculated reaction energy for the arylation process from Au_{15}-SR to Au_{15}-Ph was determined to be −33.85 kcal mol^{-1}, suggesting that the reaction $[Au_{15}(DPPOE)_3(SR)_6]^+ + 2Ph^* \rightarrow [Au_{15}(DPPOE)_3(SR)_4Ph_2]^+ + 2SR^*$ is very favorable; in other words, each Au-Ph bond was about 17 kcal mol^{-1} more stable than the corresponding Au-SR bond. This finding corroborated our experimental strategy of using phenyl groups to displace the weekly bonded -SR groups on Au_{15}-SR. To understand the origin of the higher stability of Au_{15}-Ph *vs.* Au_{15}-SR, we analyzed the frontier orbitals of the two clusters. As can be seen from Fig. 3, the Au_{15}-Ph cluster has a slighter larger band gap and a lower HOMO level, indicating its higher stability. More importantly, although both clusters are eight-electron systems according to the superatomic complex model, their HOMO orbitals exhibit very different characteristics: the HOMO of Au_{15}-SR is dominated by the two weakly bound SR groups, while that of Au_{15}-Ph features a combination of the P-type superatomic orbital of the metal core and the -Ph ligands. In other words, the more covalent or conjugated interactions between Au_{15} and the two -Ph ligands *via* the Au–C bonds stabilized the cluster, while the two -SR groups had weaker interactions with the valence electrons of the cluster core. The charge density difference plot of the Au_{15}-Ph cluster confirmed the strong charge accumulation between the Au and C atom centers due to the formation of the covalent Au–C bond (Fig. S28†).

Considering the nuanced differences in ligands between Au_{15}-SR and Au_{15}-Ph nanoclusters, we investigated their capability in electrochemically reducing CO_2 to CO (CO_2RR). The electrocatalytic CO_2RR was selected as the model reaction due to the outstanding efficiency of gold in this process and the promising prospects it offers for both fundamental and practical investigations.[63] The linear sweep voltammetry (LSV) results revealed that Au_{15}-SR displayed a higher current density and a lower onset potential than Au_{15}-Ph in CO_2-saturated

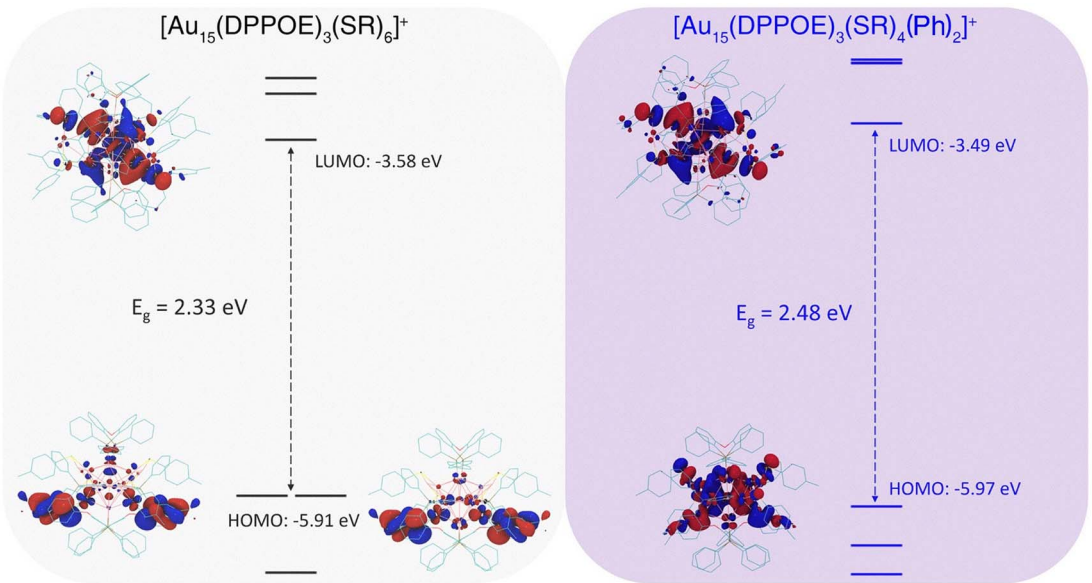

Fig. 3 Frontier orbital analyses of nanoclusters. Orbital diagram and HOMO/LUMO orbitals of $[Au_{15}(DPPOE)_3(SR)_6]^+$ (left) and $[Au_{15}(DPPOE)_3(SR)_4(Ph)_2]^+$ nanoclusters (right).

aqueous 0.5 M $KHCO_3$ solution, indicating that the Au_{15}-Ph cluster-based catalyst showed lower CO_2RR efficiency relative to Au_{15}-SR (Fig. 4A). Then, we gathered the gas products produced by the CO_2RR process and analyzed them by gas chromatography (GC). Gas chromatography detected only H_2 and CO in gas products, demonstrating a total faradaic efficiency (FE) of approximately 100% for CO and H_2. As depicted in Fig. 4B, the potential-dependent FE for CO formation was analyzed for two Au_{15} nanoclusters. Au_{15}-SR revealed a slightly higher selectivity for CO production, achieving the highest remarkable FE_{CO} over 96.2% at −0.7 V, compared to 92.9% for Au_{15}-Ph. In other words, Au_{15}-SR and Au_{15}-Ph nanoclusters generated CO across all potentials, but Au_{15}-SR exhibited slightly higher CO production than Au_{15}-Ph (Fig. 4B). In addition, the CO partial current density activity for both Au_{15}-SR and Au_{15}-Ph nanoclusters increased with growing overpotentials (Fig. 4C). Notably, Au_{15}-SR exhibited approximately a two-fold enhancement over Au_{15}-Ph at −0.8 or 0.7 V. The CO production efficiency of Au_{15}-SR was much higher than that of Au_{15}-Ph, showing a comparable turnover frequency (TOF) of the two nanoclusters (Fig. S29†). Additionally, electrochemical impedance spectroscopy (EIS) was performed on Au_{15}-SR and Au_{15}-Ph to access charge-transfer resistance, and the Au_{15}-SR nanocluster exhibited a remarkably smaller semi-circular arc, suggesting its faster electrode kinetics (Fig. 4D). We proposed that the homogeneity of the Au_{15}-SR cluster molecule resulted in smaller charge transfer resistance of the electrolyte and the catalyst, thereby making it easier for electrons to penetrate the catalyst. Furthermore, the electrocatalytic stability of Au_{15}-SR and Au_{15}-Ph was tested at −0.7 V, both showing high robustness over 8 hours (Fig. S30†), further evidenced by their maintained UV-vis, XPS, and transmission electron microscopy results (Fig. S31–S33†).

DFT calculations were then carried out to understand the CO_2RR mechanism of Au_{15}-SR and Au_{15}-Ph nanoclusters. Following previous studies on the electrocatalysis of gold nanoclusters, the active Au site was created by dethiolating one -SR ligand from nanoclusters.[64,65] For Au_{15}-SR, dethiolating the independently anchored ligand was energetically more favorable by 0.76 eV compared to the staple motif ligands (Fig. S34†), leaving the top Au atom from the Au_{13} kernel as the active site (Fig. 5A). By comparison, for Au_{15}-Ph, the active site was located on the undercoordinated Au atom from the staple motif after dethiolation (Fig. 5B). The Gibbs free energy profile in Fig. 5C shows that CO_2 reduction with Au_{15}-SR was thermodynamically more favorable due to the weaker adsorption of intermediates and the lower limiting potential of 0.43 eV, while the stronger adsorption of *CO with Au_{15}-Ph led to a higher limiting potential of 0.77 eV for CO desorption. The calculation results

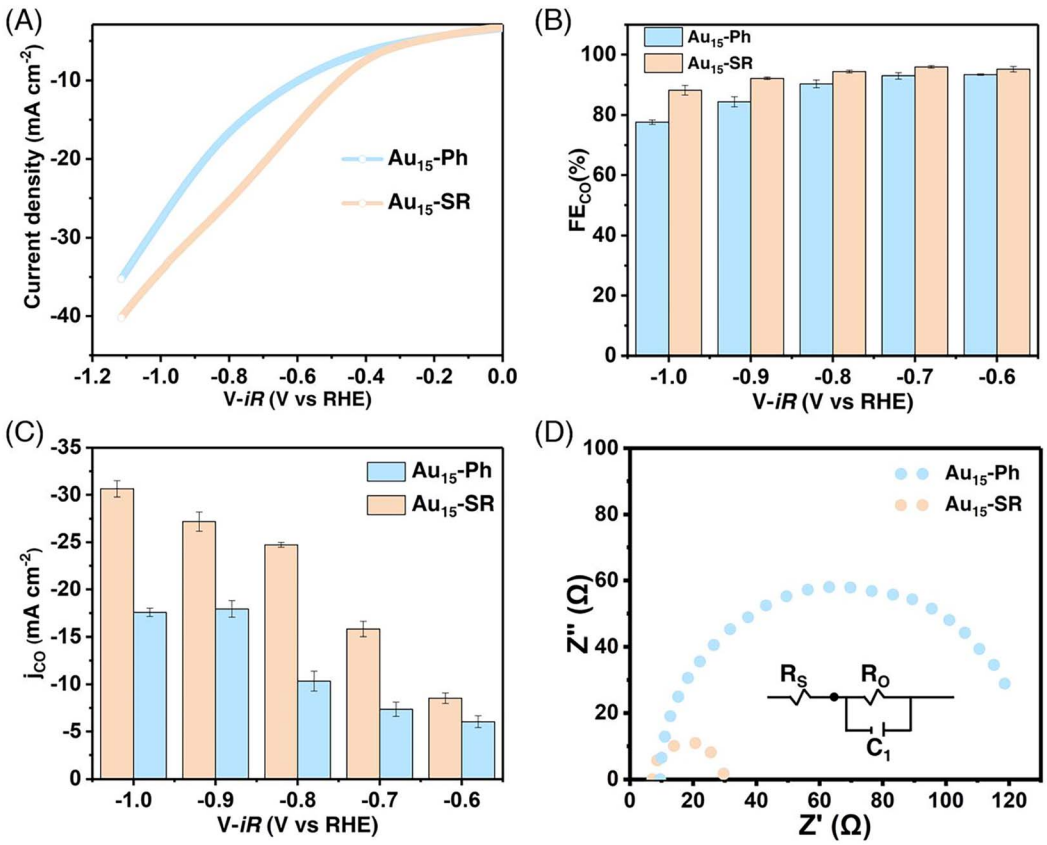

Fig. 4 Electrochemical performance of Au_{15}-SR and Au_{15}-Ph nanoclusters. (A) The LSV of Au_{15}-SR and Au_{15}-Ph nanoclusters. (B) The CO faradaic efficiency within the range of −1 to −0.6 V *vs.* the reversible hydrogen electrode (RHE). (C) The CO partial current density (j_{CO}). (D) The EIS of Au_{15}-SR and Au_{15}-Ph nanoclusters.

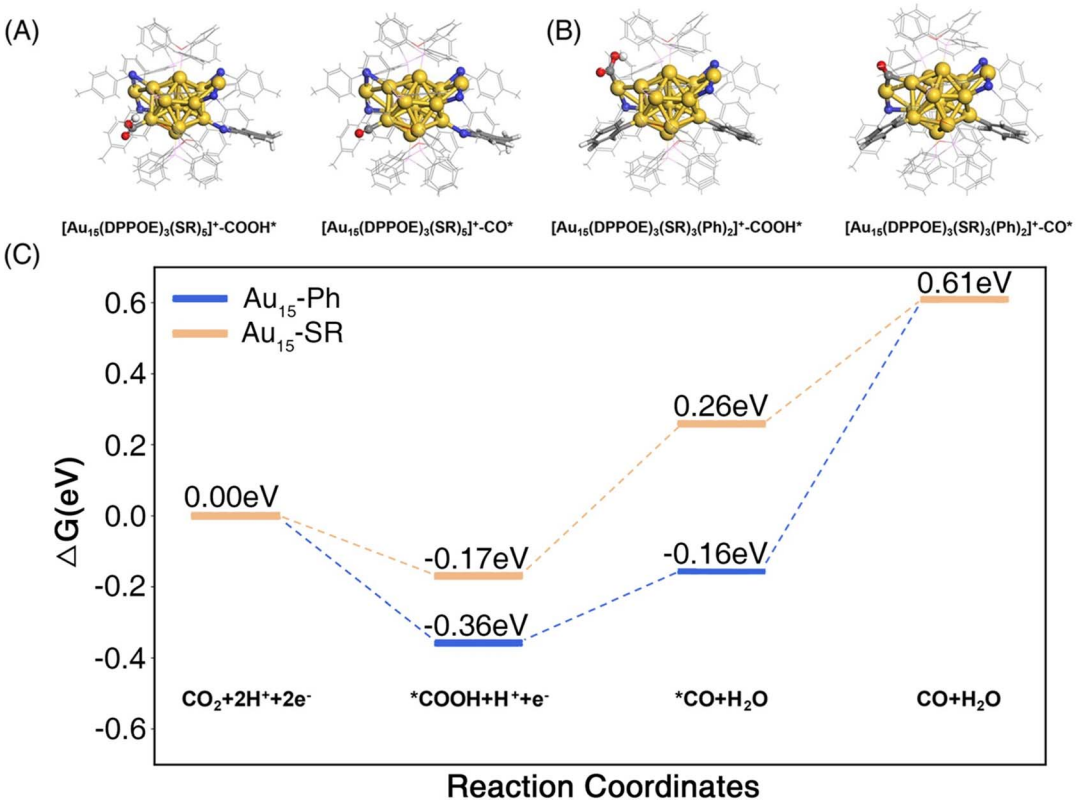

Fig. 5 DFT-optimized structures and the corresponding energetics of CO_2RR. (A) Optimized structures of *COOH and *CO intermediates for singly dethiolated $[Au_{15}(DPPOE)_3(SR)_3(Ph)_2]^+$ and (B) singly dethiolated $[Au_{15}(DPPOE)_3(SR)_5]^+$ nanoclusters. (C) Free energy profile of the CO_2RR on dethiolated $[Au_{15}(DPPOE)_3(SR)_3(Ph)_2]^+$ (blue color) and $[Au_{15}(DPPOE)_3(SR)_5]^+$ (red color) nanoclusters at 0 V *vs.* RHE.

suggested that it is more favorable to form CO in Au_{15}-SR than in Au_{15}-Ph, in agreement with the experimental observations.

3 Conclusions

In summary, the arylation of gold nanoclusters has been accomplished. The Au_{15}-SR nanocluster carried two detachable thiolate ligands on its surface, accounting for the instability of the cluster framework. On the positive side, the active surface environment of Au_{15}-SR endowed this nanocluster with high catalytic capacity towards the C–B bond cleavage of tetraarylborates. The subsequently generated dissociative aryl groups would activate the surface structure of Au_{15}-SR by anchoring aryl ligands onto the cluster kernel *via* Au-aryl interactions, giving rise to an arylgold Au_{15}-Ph nanocluster. Besides, two cluster derivatives of arylgold Au_{15}-Ph were developed by functionalizing the aryl ligands with halide substituents. In addition, DFT calculations confirmed the thermodynamic driving force underlying the arylation process from Au_{15}-SR to Au_{15}-Ph and rationalized the higher stability of the Au_{15}-Ph cluster by comparing its frontier orbitals with those of Au_{15}-SR. Furthermore, both Au_{15} cluster-based nanocatalysts displayed comparable faradaic efficiency in CO_2RR, while Au_{15}-SR exhibited superior CO generation efficiency over Au_{15}-Ph, as derived from experimental results and rationalized by theoretical calculations. Overall, the findings in this work have significant implications for research in both metal nanoclusters and arylgold complexes, and we hope these observations will provide valuable insights for further studies of arylgold nanoclusters.

Data availability

The data that support the findings of this study are available in the ESI† of this article.

Author contributions

C. Zhu conceived and carried out the experiments. B. Li performed the theoretical simulations. C. Li, L. Lu, H. Li, and X. Yuan assisted in the synthesis and CO_2RR measurements. X. Kang, D.-e. Jiang, and M. Zhu supervised the project. All authors commented on and agreed to the manuscript.

Conflicts of interest

There are no conflicts to declare.

Acknowledgements

We acknowledge the financial support from the NSFC (22371003, 22101001, and 22471001), the Ministry of Education, Natural Science Foundation of Anhui Province (2408085Y006),

the University Synergy Innovation Program of Anhui Province (GXXT-2020-053), and the Scientific Research Program of Universities in Anhui Province (2022AH030009). D.-e. Jiang acknowledges Vanderbilt University for support.

Notes and references

1 R. Jin, C. Zeng, M. Zhou and Y. Chen, *Chem. Rev.*, 2016, **116**, 10346–10413.
2 I. Chakraborty and T. Pradeep, *Chem. Rev.*, 2017, **117**, 8208–8271.
3 N. A. Sakthivel and A. Dass, *Acc. Chem. Res.*, 2018, **51**, 1774–1783.
4 W. Kurashige, Y. Niihori, S. Sharma and Y. Negishi, *Coord. Chem. Rev.*, 2016, **320**, 238–250.
5 S. Kenzler and A. Schnepf, *Chem. Sci.*, 2021, **12**, 3116–3129.
6 J. Yan, B. K. Teo and N. Zheng, *Acc. Chem. Res.*, 2018, **51**, 3084–3093.
7 Z. Liu, H. Tan, B. Li, Z. Hu, D.-e. Jiang, Q. Yao, L. Wang and J. Xie, *Nat. Commun.*, 2023, **14**, 3374.
8 W.-D. Si, C. Zhang, M. Zhou, W.-D. Tian, Z. Wang, Q. Hu, K.-P. Song, L. Feng, X.-Q. Huang, Z.-Y. Gao, C.-H. Tung and D. Sun, *Sci. Adv.*, 2023, **9**, eadg3587.
9 P. Luo, X.-J. Zhai, S. Bai, Y.-B. Si, X.-Y. Dong, Y.-F. Han and S.-Q. Zang, *Angew. Chem., Int. Ed.*, 2023, **62**, e202219017.
10 J. Zhao, A. Ziarati, A. Rosspeintner and T. Bürgi, *Angew. Chem., Int. Ed.*, 2023, **63**, e202316649.
11 J. Tang, S. Zhang, B.-W. Zhou, W. Wang and L. Zhao, *J. Am. Chem. Soc.*, 2023, **145**, 23442–23451.
12 X.-L. Pei, P. Zhao, H. Ube, Z. Lei, K. Nagata, M. Ehara and M. Shionoya, *J. Am. Chem. Soc.*, 2022, **144**, 2156–2163.
13 W. Fei, S. Antonello, T. Dainese, A. Dolmella, M. Lahtinen, K. Rissanen, A. Venzo and F. Maran, *J. Am. Chem. Soc.*, 2019, **141**, 16033–16045.
14 G. Yang, Z. Wang, F. Du, F. Jiang, X. Yuan and J. Y. Ying, *J. Am. Chem. Soc.*, 2023, **145**, 11879–11898.
15 C. Zhou, M. Wang, Q. Yao, Y. Zhou, C. Hou, J. Xia, Z. Wang, J. Chen and J. Xie, *Aggregate*, 2024, **5**, e401.
16 Z. Liu, J. Chen, B. Li, D.-e. Jiang, L. Wang, Q. Yao and J. Xie, *J. Am. Chem. Soc.*, 2024, **146**, 11773–11781.
17 H. Häkkinen and M. Walter, *J. Phys. Chem. B*, 2006, **110**, 9927–9931.
18 Y. Horita, S. Hossain, M. Ishimi, P. Zhao, M. Sera, T. Kawawaki, S. Takano, Y. Niihori, T. Nakamura, T. Tsukuda, M. Ehara and Y. Negishi, *J. Am. Chem. Soc.*, 2023, **145**, 23533–23540.
19 C. P. Joshi, M. S. Bootharaju, M. J. Alhilaly and O. M. Bakr, *J. Am. Chem. Soc.*, 2015, **137**, 11578–11581.
20 Y. Li and R. Jin, *J. Am. Chem. Soc.*, 2020, **142**, 13627–13644.
21 Z. Xu, H. Dong, W. Gu, Z. He, F. Jin, C. Wang, Q. You, J. Li, H. Deng, L. Liao, D. Chen, J. Yang and Z. Wu, *Angew. Chem., Int. Ed.*, 2023, **62**, e202308441.
22 G. Soldan, M. A. Aljuhani, M. S. Bootharaju, L. G. AbdulHalim, M. R. Parida, A.-H. Emwas, O. F. Mohammed and O. M. Bakr, *Angew. Chem., Int. Ed.*, 2016, **55**, 5749.
23 Y. Zhang, S.-R. He, Y. Yang, T.-S. Zhang, Z.-M. Zhu, W. Fei and M.-B. Li, *J. Am. Chem. Soc.*, 2023, **145**, 12164–12172.
24 T.-H. Chiu, J.-H. Liao, Y.-Y. Wu, J.-Y. Chen, Y. Chen, X. Wang, S. Kahlal, J.-Y. Saillard and C. W. Liu, *J. Am. Chem. Soc.*, 2023, **145**, 16739–16747.
25 V. Rück, N. K. Mishra, K. K. Sørensen, M. B. Liisberg, A. B. Sloth, C. Cerretani, C. B. Mollerup, A. Kjaer, C. Lou, K. J. Jensen and T. Vosch, *J. Am. Chem. Soc.*, 2023, **145**, 16771–16777.
26 M. Suyama, S. Takano and T. Tsukuda, *J. Am. Chem. Soc.*, 2023, **145**, 3361–3368.
27 N. A. Sakthivel, M. Shabaninezhad, L. Sementa, B. Yoon, M. Stener, R. L. Whetten, G. Ramakrishna, A. Fortunelli, U. Landman and A. Dass, *J. Am. Chem. Soc.*, 2020, **142**, 15799–15814.
28 L.-J. Liu, F. Alkan, S. Zhuang, D. Liu, T. Nawaz, J. Guo, X. Luo and J. He, *Nat. Commun.*, 2023, **14**, 2397.
29 X. Kang, X. Wei, S. Wang and M. Zhu, *Inorg. Chem.*, 2020, **59**, 8736–8743.
30 J. Chen, Q.-F. Zhang, T. A. Bonaccorso, P. G. Williard and L.-S. Wang, *J. Am. Chem. Soc.*, 2014, **136**, 92–95.
31 D. Arima and M. Mitsui, *J. Am. Chem. Soc.*, 2023, **145**, 6994–7004.
32 Y. Shichibu, Y. Negishi, T. Watanabe, N. K. Chaki, H. Kawaguchi and T. Tsukuda, *J. Phys. Chem. C*, 2007, **111**, 7845–7847.
33 Z.-H. Gao, J. Dong, Q.-F. Zhang and L.-S. Wang, *Nanoscale Adv.*, 2020, **2**, 4902–4907.
34 J.-J. Li, Z.-J. Guan, S.-F. Yuan, F. Hu and Q.-M. Wang, *Angew. Chem., Int. Ed.*, 2021, **60**, 6699.
35 N. Kobayashi, Y. Kamei, Y. Shichibu and K. Konishi, *J. Am. Chem. Soc.*, 2013, **135**, 16078–16081.
36 J.-J. Li, Z. Liu, Z.-J. Guan, X.-S. Han, W.-Q. Shi and Q.-M. Wang, *J. Am. Chem. Soc.*, 2022, **144**, 690–694.
37 L. Qin, F. Sun, X. Ma, G. Ma, Y. Tang, L. Wang, Q. Tang, R. Jin and Z. Tang, *Angew. Chem., Int. Ed.*, 2021, **60**, 26136–26141.
38 M. R. Narouz, K. M. Osten, P. J. Unsworth, R. W. Y. Man, K. Salorinne, S. Takano, R. Tomihara, S. Kaappa, S. Malola, C.-T. Dinh, J. D. Padmos, K. Ayoo, P. J. Garrett, M. Nambo, J. H. Horton, E. H. Sargent, H. Häkkinen, T. Tsukuda and C. M. Crudden, *Nat. Chem.*, 2019, **11**, 419–425.
39 H. Shen, G. Deng, S. Kaappa, T. Tan, Y.-Z. Han, S. Malola, S.-C. Lin, B. K. Teo, H. Häkkinen and N. Zheng, *Angew. Chem., Int. Ed.*, 2019, **58**, 17731–17735.
40 V. K. Kulkarni, B. N. Khiarak, S. Takano, S. Malola, E. L. Albright, T. I. Levchenko, M. D. Aloisio, C.-T. Dinh, T. Tsukuda, H. Häkkinen and C. M. Crudden, *J. Am. Chem. Soc.*, 2022, **144**, 9000–9006.
41 S.-F. Yuan, Z. Lei, Z.-J. Guan and Q.-M. Wang, *Angew. Chem., Int. Ed.*, 2021, **60**, 5225–5229.
42 S.-F. Yuan, C.-Q. Xu, J. Li and Q.-M. Wang, *Angew. Chem., Int. Ed.*, 2019, **58**, 5906–5909.
43 X. Kang and M. Zhu, *Chem. Mater.*, 2019, **31**, 9939–9969.
44 C. A. Hosier and C. J. Ackerson, *J. Am. Chem. Soc.*, 2019, **141**, 309–314.

45 S. Kenzler, F. Fetzer, C. Schrenk, N. Pollard, A. R. Frojd, A. Z. Clayborne and A. Schnepf, *Angew. Chem., Int. Ed.*, 2019, **58**, 5902–5905.
46 Q.-F. Zhang, X. Chen and L.-S. Wang, *Acc. Chem. Res.*, 2018, **51**, 2159–2168.
47 H. Yang, Y. Wang, J. Yan, X. Chen, X. Zhang, H. Häkkinen and N. Zheng, *J. Am. Chem. Soc.*, 2014, **136**, 7197–7200.
48 P. N. Gunawardene, J. F. Corrigan and M. S. Workentin, *J. Am. Chem. Soc.*, 2019, **141**, 11781–11785.
49 X.-K. Wan, Z.-J. Guan and Q.-M. Wang, *Angew. Chem., Int. Ed.*, 2017, **56**, 11494–11497.
50 A. Genoux, M. Biedrzycki, E. Merino, E. Rivera-Chao, A. Linden and C. Nevado, *Angew. Chem., Int. Ed.*, 2021, **60**, 4164–4168.
51 M.-C. Tang, C.-H. Lee, S.-L. Lai, M. Ng, M.-Y. Chan and V. W.-W. Yam, *J. Am. Chem. Soc.*, 2017, **139**, 9341–9349.
52 M.-C. Tang, M.-Y. Leung, S.-L. Lai, M. Ng, M.-Y. Chan and V. W.-W. Yam, *J. Am. Chem. Soc.*, 2018, **140**, 13115–13124.
53 L. Laurentius, S. R. Stoyanov, S. Gusarov, A. Kovalenko, R. Du, G. P. Lopinski and M. T. McDermott, *ACS Nano*, 2011, **5**, 4219–4227.
54 F. Mirkhalaf, J. Paprotny and D. J. Schiffrin, *J. Am. Chem. Soc.*, 2018, **128**, 7400–7401.
55 A. Laguna, M. Laguna, M. C. Gimeno and P. G. Jones, *Organometallics*, 1992, **11**, 2759–2760.
56 W.-D. Si, C. Zhang, M. Zhou, Z. Wang, L. Feng, C.-H. Tung and D. Sun, *Sci. Adv.*, 2024, **10**, eadm6928.
57 A. Sladek, S. Hofreiter, M. Paul and H. Schmidbaur, *J. Organomet. Chem.*, 1995, **501**, 47–51.
58 H. Salem, L. J. W. Shimon, G. Leitus, L. Weiner and D. Milstein, *Organometallics*, 2008, **27**, 2293–2299.
59 W. V. Konze, B. L. Scott and G. J. Kubas, *Chem. Commun.*, 1999, 1807–1808.
60 M. Joost, A. Amgoune and D. Bourissou, *Angew. Chem., Int. Ed.*, 2015, **54**, 15022–15045.
61 F. Yue, H. Ma, P. Ding, H. Song, Y. Liu and Q. Wang, *ACS Cent. Sci.*, 2023, **9**, 2268–2276.
62 C. Zhu, J. Xin, J. Li, H. Li, X. Kang, Y. Pei and M. Zhu, *Angew. Chem., Int. Ed.*, 2022, **61**, e202205947.
63 B. Kumar, T. Kawawaki, N. Shimizu, Y. Imai, D. Suzuki, S. Hossain, L. V. Naira and Y. Negishi, *Nanoscale*, 2020, **12**, 9969–9979.
64 D. R. Alfonso, D. Kauffman and C. Matranga, *J. Chem. Phys.*, 2016, **144**, 184705.
65 F. Sun, L. Qin, Z. Tang, G. Deng, M. S. Bootharaju, Z. Wei, Q. Tang and T. Hyeon, *Chem. Sci.*, 2023, **14**, 10532–10546.